Ocean Engineering 260 (2022) 111973

Contents lists available at ScienceDirect

Ocean Engineering

journal homepage: www.elsevier.com/locate/oceaneng

# Numerical validation of simple non-stationary models for self-propelled pitching foils

R. Fernandez-Feria *, E. Sanmiguel-Rojas, P.E. Lopez-Tello

*Fluid Mechanics, Universidad de Málaga, Dr Ortiz Ramos s/n, 29071 Málaga, Spain*

ARTICLE INFO

*Keywords:*
self-propulsion
Aquatic locomotion
Swimming
Flapping foil

ABSTRACT

High-resolution numerical simulations of the self propelled locomotion of two-dimensional pitching foils are used to assess simplified models based on linear potential theory for the fluid-foil interaction. These models are very useful because they provide simple analytical estimations of the swimming velocity, among other relevant features of the aquatic locomotion of fishes and underwater robotic devices propelled by flapping foils. In particular, we consider a pitching foil self-propelled from two different models of the unsteady thrust force based on linear potential theory, both complemented with a new simple model for the unsteady viscous friction obtained from the present full-numerical simulations, valid in a wide range of Reynolds numbers ($10^3 \lesssim Re \lesssim 10^4$) of interest for many natural and robotic swimmers. The resulting ordinary differential equation for the swimming velocity is easily integrated numerically, comparing favorably with the full-numerical simulations for small pitch amplitudes (Strouhal numbers $St \lesssim 0.25$) and the above range of Reynolds numbers. Further, when the swimming velocity is small, simple approximate solutions of the dynamic model equation are obtained, whose pitch amplitude validity range is more limited than the numerical solution of the model as the Reynolds number and the foil mass ratio increase, becoming negligibly small when the frequency-based Reynolds number is well over $10^4$. Although both thrust models yield similar quantitative results, they predict qualitatively different dependencies of the swimming velocity on the different non-dimensional parameters.

## 1. Introduction

Many natural swimmers use flapping fins and tails for their locomotion (Webb, 1975; Alexander, 2003). This common strategy for natural aquatic locomotion has motivated researchers around the world to analyze the efficient thrust generation of rigid flapping foils during the past few decades (Lighthill, 1970; Wu, 1971; Triantafyllou et al., 1993; Anderson et al., 1998; Young and Lai, 2007; Mackowski and Williamson, 2015; Fernandez-Feria, 2017; Paniccia et al., 2021), and to develop bioinspired underwater vehicles self propelled by flapping foils (Triantafyllou and Triantafyllou, 1995; Lauder et al., 2007; Wen et al., 2012; Gibouin et al., 2018; Zhu et al., 2019; Sánchez-Rodríguez et al., 2021).

Of special relevance for the last mentioned purpose is the development of simple, but reliable models for self-propelled flapping locomotion. Particularly, numerical simulations show that two-dimensional rigid foils self-propel when actuated by a heaving or/and a pitching motion (Alben and Shelley, 2005; Spagnolie et al., 2010; Zhang et al., 2010; Das et al., 2019; Lin et al., 2021; Benetti Ramos et al., 2021). These results are of great interest because two-dimensional, rigid flapping foils model the oscillatory motion of the caudal fins of certain fishes and of their biomimetic robotic counterparts (Lighthill, 1969; Smits, 2019). Based on these numerical simulations and on experimental data from very different sources, several scaling laws have been derived characterizing aquatic locomotion by flapping foils; i.e., the time-averaged final swimming velocity in terms of the Strouhal and the Reynolds numbers (to be defined below) and other related non-dimensional parameters (Triantafyllou et al., 2005; Eloy, 2012; Gazzola et al., 2014; Floryan et al., 2017; Saadat et al., 2017; Lin et al., 2021; Das et al., 2022).

However, simple models for the unsteady swimming velocity, not only for its time-averaged value, are scarce. Sánchez-Rodríguez et al. (2020) considered the self-propulsion of a rigid pitching foil using the results of Theodorsen (1935) and Garrick (1936) from linear potential theory for the unsteady lift and thrust forces exerted by the fluid on the foil. These authors complemented these inviscid forces with a constant drag coefficient $C_D$. Since the final swimming velocity, both its time averaged value and its oscillations around the mean, strongly depends

* Corresponding author.
*E-mail addresses:* ramon.fernandez@uma.es (R. Fernandez-Feria), enrique.sanmiguel@uma.es.com (E. Sanmiguel-Rojas), pe.lopeztello@uma.es (P.E. Lopez-Tello).

https://doi.org/10.1016/j.oceaneng.2022.111973
Received 1 March 2022; Received in revised form 8 June 2022; Accepted 8 July 2022
Available online 16 July 2022

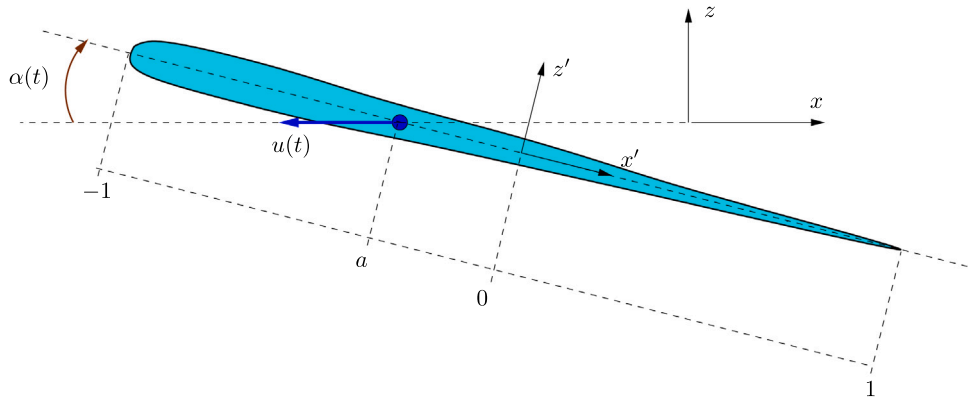


**Fig. 1.** Sketch of the self-propelled foil (dimensionless quantities).

on the skin friction drag, which is not constant for an oscillatory foil, the results from the model cannot properly be compared with viscous numerical simulations of a self-propelled pitching foil. One of the goals of the present work is to develop such a model for the unsteady viscous drag coefficient, $C_D(t)$, obtained from full-numerical simulations of a self-propelled pitching foil in the Reynolds number's range of interest for many natural and robotic swimmers. This unsteady viscous drag will be combined with two different formulations of the thrust force from the linear potential theory (Garrick, 1936; Fernandez-Feria, 2016) to develop simple non-stationary models for the self-propulsion of rigid pitching foils. The other main goal of the present work is to compare the results from these two simple unsteady models with high-resolution numerical simulations to assess their approximate range of validity, if any. The simplified model provides approximate analytical results not only for the time-averaged swimming velocity, but also for the amplitude, frequency and phase of its oscillations, and for the transient time needed to reach the final cruising state.

The novelty of the present work is thus to combine a non-stationary model for the unsteady viscous drag of a self-propelled pitching foil, developed in the present work from accurate numerical simulations, with two analytical expressions for the unsteady thrust force from linear potential theory to obtain simple analytical approximations for the non-stationary swimming velocity by solving with novel analytical techniques the resulting self-propulsion equations. These analytical expressions are then validated with the results from high resolution numerical simulations. The only work to the authors' knowledge that develop a similar analytical approximation for the unsteady swimming velocity of a self-propelled pitching foil is that of Sánchez-Rodríguez et al. (2020), but using just one of the two previous expressions for the unsteady thrust force and, what is more relevant in the context of the present work, a constant value for the drag coefficient, which prevents its quantitative comparison with full numerical simulations of a self-propelled pitching foil. The comparison of the two self-propulsion models with numerical results given in the present work provides an assessment of their limitations in terms of the different non-dimensional parameters, such as the pitch amplitude, the frequency-based Reynolds number and the mass ratio of the foil.

## 2. Formulation

We consider an underwater, self propelled swimmer consisting of just a two-dimensional hydrofoil of mass $m$ per unit span and chord length $c$. The swimming propulsion is triggered by an imposed sinusoidal pitching motion,

$$\alpha = \alpha_0 \sin(\omega \tilde{t}) , \tag{1}$$

about a given pivot axis $a$, where $\alpha_0$ and $\omega$ are the pitching amplitude and frequency, respectively, and $\tilde{t}$ is the (dimensional) time (we use a *tilde* ˜ to distinguish dimensional quantities from their dimensionless counterparts when written with the same letter). To facilitate the full numerical simulation described below in Section 3, the center of mass coincides with the pivot point and it is constrained to move only along the $x$ axis, from which $\alpha$ is measured clockwise (see Fig. 1); i.e., heaving motion of the foil is not considered. This inhibition of the heaving motion will obviously reduce the propulsion capabilities of the hydrofoil (Sánchez-Rodríguez et al., 2020; Das et al., 2022), but it will not affect to the validation purposes of the present work.

Non-dimensional variables are used in what follows, except specified otherwise, scaling lengths with the semi-chord length $c/2$, time with $\omega^{-1}$ and mass through the fluid density $\rho$. Thus, $t = \omega \tilde{t}$ is the non-dimensional time and the hydrofoil spans from $x' = -1$ to $x' = 1$ in the coordinates $(x', y')$ attached to the mid-chord point of the foil (see Fig. 1). The center of mass and pivot point are located at $x' = a$, with $a = -1$ corresponding to the leading edge and $a = 1$ to the trailing edge. The non-dimensional swimming velocity $u(t)$, considered positive when directed towards the negative $x$ axis of the absolute coordinates system $(x, y)$, is actually the inverse of the reduced frequency $k(t)$ commonly used in unsteady aerodynamics (e.g., Theodorsen, 1935), now depending on time,

$$u(t) = \frac{2\tilde{u}}{\omega c} = \frac{1}{k(t)} , \tag{2}$$

where $\tilde{u}(\tilde{t})$ is its dimensional counterpart. In the numerical simulations (Section 3) the foil is a flat plate with the pivot (and center of mass) located at the leading edge ($a = -1$). However, the theoretical models of the subsequent sections are general for any slender foil as that depicted in Fig. 1.

The motion of the foil is governed by Newton's second law applied to the center of mass, which in dimensionless form can be written as

$$R\,\dot{u} = -\hat{C}_x , \tag{3}$$

where

$$R = \frac{4m}{\pi \rho c^2} \tag{4}$$

is the non-dimensional mass of the hydrofoil, a dot denotes a derivative with respect to the dimensionless time, and

$$\hat{C}_x = \frac{8F_x}{\pi \rho c^3 \omega^2} = \frac{u^2 C_x}{\pi} \tag{5}$$

is the $x$-component of the non-dimensional force per unit span that the fluid exerts on the foil. We use a 'hat' in $\hat{C}_x$ to remark that this is not the standard coefficient associated to the force $F_x$, $C_x = F_x/(\frac{1}{2}\rho \tilde{u}^2 c)$, which is also included in the relation (5) for comparison's sake.

To obtain $\hat{C}_x$ one has to solve the incompressible Navier–Stokes (N–S) equations, which in non-dimensional form can be written as

$$\boldsymbol{\nabla} \cdot \mathbf{w} = 0 , \qquad \frac{\partial \mathbf{w}}{\partial t} + \mathbf{w} \cdot \boldsymbol{\nabla} \mathbf{w} = -\boldsymbol{\nabla} p + \frac{1}{Re_\omega} \nabla^2 \mathbf{w} , \tag{6}$$

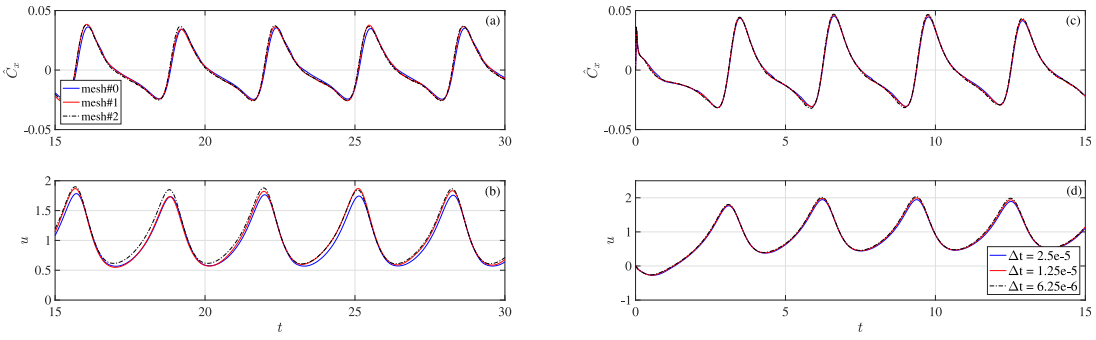


**Fig. 2.** Mesh (a)–(b) and time-step (c)–(d) convergence studies in terms of the non-dimensional time evolutions of the non-dimensional force per unit span (top) and the non-dimensional swimming velocity (bottom) for $\alpha_0 = 0.2\,(\simeq 11.46$ deg), $f = 2$ Hz and $R = 0.02$ in water ($Re_\omega \simeq 1.25\times 10^5$).

where $\mathbf{w}$ is the non-dimensional fluid velocity field (scaled with $\omega c/2$), $p$ is the non-dimensional pressure field (scaled with $\rho\omega^2 c^2/4$), and a Reynolds number based on the frequency and the chord-length has been defined,

$$Re_\omega = \frac{\rho\omega c^2}{4\mu}, \tag{7}$$

with $\mu$ the fluid viscosity. These equations have to be solved with no-slip boundary conditions on the foil surface, which moves according to (1), which in dimensionless form reads $\alpha = \alpha_0 \sin t$, and Eq. (3). The numerical resolution of the problem is described in Section 3 below. The results from these numerical simulations will be used to assess the validity range of the model described in Sections 5 and 6. The model is based on the linear potential flow theory, for which analytical expressions for the thrust coefficient $\hat{C}_T(t)$, corresponding to $-\hat{C}_x(t)$ but without viscous friction forces, are provided. In fact we shall compare with the results from two different analytical expressions for $\hat{C}_T(t)$, and from two approaches for each thrust model, the first one by integrating numerically the ODE resulting from Eq. (3), and the second one by using approximate analytical solutions of this equation.

Once Eq. (3) is solved for a given initial condition, its solution $u(t)$ will eventually reach a final or *permanent* state consisting of an oscillatory periodic motion around a mean, or time-averaged, value $U_\infty \equiv \overline{u}(t\to\infty)$ (see, e.g., Fig. 4 in Section 4 below; time-averaged quantities in this permanent state are denoted with an over bar, see Eq. (11) in Section 4 below for the exact definition). The corresponding time-averaged reduced frequency is

$$k_\infty = \frac{1}{U_\infty}. \tag{8}$$

Of particular interest for the locomotion through flapping foils is the corresponding Strouhal number (Triantafyllou et al., 1991; Taylor et al., 2003; Gazzola et al., 2014), which is defined as

$$St = \frac{f\tilde{A}}{\tilde{U}_\infty} = \frac{A}{2\pi U_\infty}, \tag{9}$$

where $f = \omega/(2\pi)$ is the actuation frequency in Hertz, $\tilde{U}_\infty$ the dimensional mean forward speed, and $\tilde{A}$ and $A$ are the dimensional and nondimensional beat amplitudes, respectively, taken as the maximum peak-to-peak trailing edge amplitude; i.e., $A = 2(1-a)\sin\alpha_0$ for the present pitching motion. Another non-dimensional parameter of interest is the Reynolds number associated to the swimming velocity:

$$Re = \frac{\rho\tilde{U}_\infty c}{\mu} = 2U_\infty Re_\omega. \tag{10}$$

## 3. Numerical method and its validation

To solve the coupled problem of fluid–structure interaction (FSI) we use the finite volume-based solver Ansys-Fluent v21.2. Specifically, the fluid part is solved using both laminar flow (as in Sanmiguel-Rojas and Fernandez-Feria, 2021) and transition $k-\omega$ SST model (Sanmiguel-Rojas and Fernandez-Feria, 2022). This turbulence model has been shown to accurately capture the laminar-turbulent transition in oscillating foils for the range of Reynolds numbers of interest in the present work (Kang et al., 2009; Karbasian and Kim, 2016; Wu et al., 2020). On the other hand, to simulate the FSI, the plate was mimicked by a user defined function (UDF), i.e., a $C$ program compiled in Fluent. Specifically, we used the Ansys-Fluent supplied function declaration DEFINE-CG-MOTION. Thanks to this $C$ macro, the pitching motion defined in Eq. (1) was imposed and, simultaneously, the motion of the foil was integrated at each time step solving Eq. (3) computationally. Details of the numerical approach and the computational domain are given in Appendix.

The plate has a length $c = 0.2$ m and a thickness $0.01c$, with rounded ends [see Fig. A.2(b) in Appendix]. The foil is thin enough to compare the numerical results with linear potential theory, which is independent of the foil profile, so that a flat plate is chosen for simplicity. We assume that all the mass of the plate is concentrated at the leading edge ($a = -1$), as outlined in Fig. A.1 in Appendix. (However, the theoretical analysis of Sections 5 and 6 is made for arbitrary values of $a$ between $-1$ and 1.) Except otherwise specified, in all the numerical simulations the fluid is water ($\rho = 998.2$ kg/m$^3$ and $\mu = 0.001003$ kg/ms), and we select the plate mass $m$ for each given mass ratio $R$. Typically, we use $R = 0.02$.

A mesh convergence study was performed with the following three meshes: mesh#0 (coarse) with 68 732 cells, 424 cells on the plate and a time step $d\tilde{t} = 5\times 10^{-5}$ s; mesh#1 (medium) with 130 103 cells, 600 on the plate and a time step $d\tilde{t} = 2.5\times 10^{-5}$ s; mesh#2 (fine) with 249 549 cells, 848 on the plate and a time step $d\tilde{t} = 1.25\times 10^{-5}$ s. The time step was set to guarantee a maximum $CFL < 1$ in all cases.

Figs. 2(a) and (b) display several final cycles of the $x-$component of the non-dimensional force per unit span and the non-dimensional velocity of the center of mass calculated with the transition turbulent model using the three meshes for one of the most unfavorable cases analyzed, corresponding to $\alpha_0 = 0.2$ and $f = 2$ Hz, with $R = 0.02$ in water ($Re_\omega \simeq 1.25\times 10^5$, resulting a time-averaged swimming velocity $U_\infty \simeq 1.06$, and $Re \simeq 2.65\times 10^5$). Note that the differences between the results computed with meshes #1 and #2 are negligible, indicating that both are very close to mesh independence. Thus, all the results included in the next sections are performed with the (medium) mesh#1, which is the one depicted in Fig. A.2 in Appendix. Additionally, a time-step convergency study was also performed with mesh #1 by halving the time step $d\tilde{t} = 2.5\times 10^{-5}$ used in the mesh convergence study: $d\tilde{t} = 2.5\times 10^{-5}, 1.25\times 10^{-5}$ and $6.25\times 10^{-6}$. Figs. 2(c) and (d) show that the results are practically indistinguishable, even for the initial cycles starting from the foil at rest where the temporal variations of $u$ are larger than later on.

Fig. 3 shows a snapshot of the non-dimensional turbulence kinetic energy at $t = 28.25$ for the case considered in Fig. 2. This instant of time corresponds to a position of the plate with $\alpha = 0$, which yields a

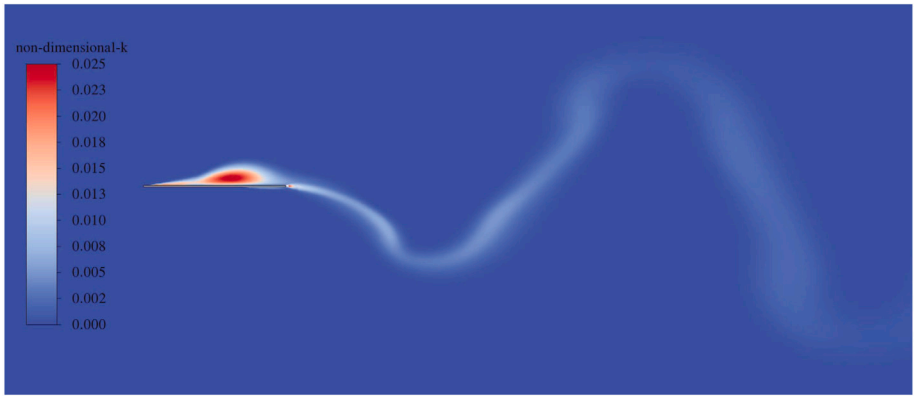


**Fig. 3.** Snapshot of the non-dimensional turbulence kinetic energy at $t = 28.25$ for the case considered in Fig. 2 computed with mesh#1.

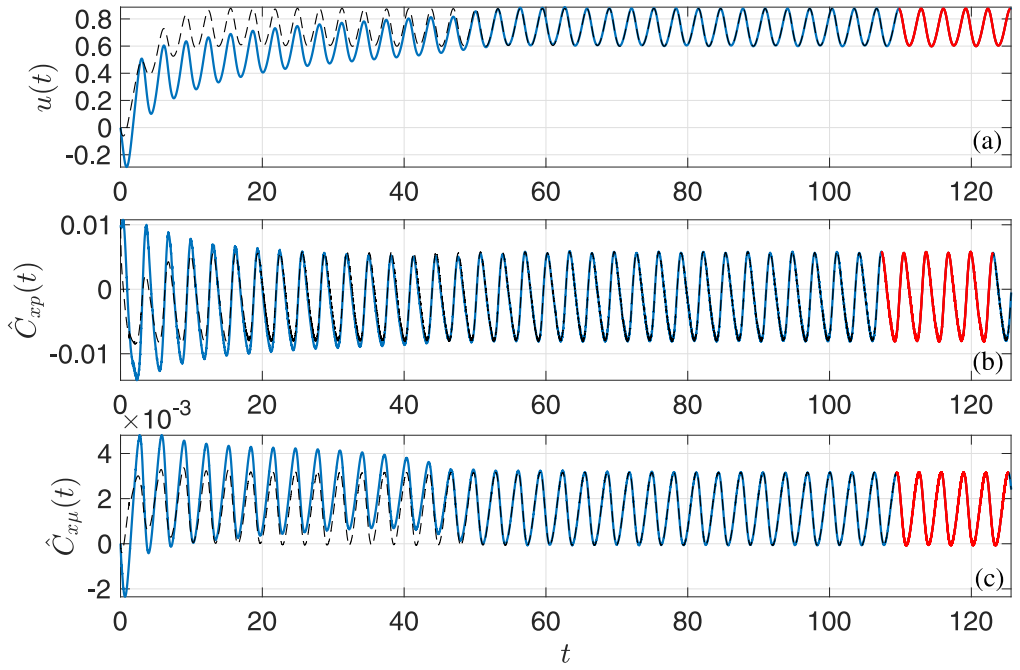


**Fig. 4.** Time evolutions of the non-dimensional swimming velocity (a), non-dimensional pressure part of the $x$-component of the force (b) and the remaining viscous part of the force (c) for $\alpha_0 = 0.1$ ($\simeq$7.73 deg), $R = 0.02$, $f = 0.5$ Hz in water ($Re_\omega \simeq 31\,266$). $Re \simeq 45\,599$. Continuous lines correspond to the results from the turbulence model, while dashed thin lines are obtained assuming laminar flow. The last 5 cycles used for time averaging are marked in red. (For interpretation of the references to color in this figure legend, the reader is referred to the web version of this article.)

local maximum in the swimming velocity. Clearly, turbulence effects are manifest at these Reynolds numbers. However, when computing the force that the fluid exerts on the foil, the result does not differ much from the value obtained with the laminar simulations in the final permanent state, especially for smaller Reynolds numbers (see Fig. 4 discussed just below for $Re \simeq 45\,000$), demonstrating that turbulence has a negligible effect on the propulsion characteristics at the frequencies and Reynolds numbers discussed in the present work. A similar conclusion was already reached in Sanmiguel-Rojas and Fernandez-Feria (2022) for a uniform flow at comparable Reynolds numbers past a NACA0012 airfoil, instead of the present self-propelled thin flat plate, but using quite similar numerical code and meshes to solve the fluid dynamics. In that reference it was shown that turbulence effects are negligible if the Strouhal number is smaller than about 0.8, a value well beyond the present numerical simulations for small pitch amplitudes. Additionally, in Sanmiguel-Rojas and Fernandez-Feria (2022) the numerical code was also validate against experimental data by Mackowski and Williamson (2015).

## 4. Numerical results. Modeling the unsteady viscous drag

The result of a typical numerical simulation is plotted in Fig. 4. The non-dimensional swimming velocity $u(t)$ starting from the foil at rest is shown together with the pressure and viscous parts of the $x-$component force, $\hat{C}_{xp}(t)$ and $\hat{C}_{x\mu}(t)$, respectively ($\hat{C}_x \equiv \hat{C}_{xp} + \hat{C}_{x\mu}$). The figure displays both the results assuming laminar flow and using the turbulence model. They almost coincide once the final or permanent oscillatory state has been reached, but differ during the transient period towards that final state. This indicates that near-wall turbulence is more important during the transient acceleration of the foil, greatly affecting to the fluid forces, but once the final state has been reached, the relevant turbulent regions are detached from the foil, as shown in Fig. 3, barely affecting to the fluid forces. All reported numerical results are computed with the turbulence model.

The time average of any quantity $\phi(t)$ at the final oscillatory state is computed using the last $n(= 5)$ cycles (marked in red in Fig. 4) as

$$\overline{\phi} = \frac{1}{nT_\phi}\int_t^{t+nT_\phi} \phi(t)dt\,, \tag{11}$$

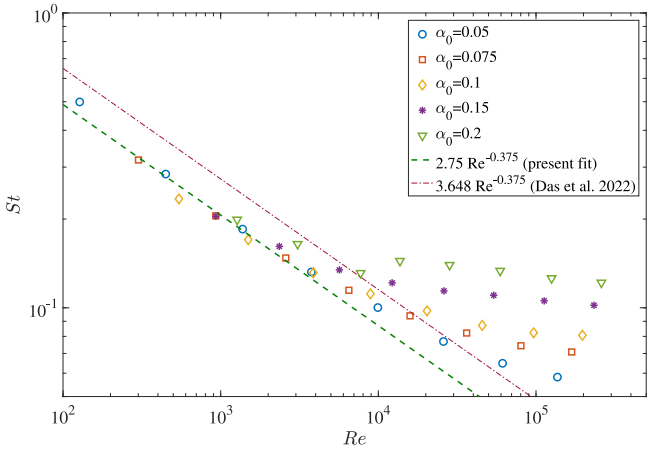


**Fig. 5.** $St - Re$ relation for all the numerical results computed with $R = 0.02$ for different values of $\alpha_0$ and $Re_\omega$ (symbols). The dashed line is a power-law fit for $Re \lesssim 2000$, and the dash-and-dot line the one obtained by Das et al. (2022) for a NACA0012 airfoil.

where $T_\phi$ is the non-dimensional oscillation period of $\phi$. Note that for $u$ and both components of $\hat{C}_x$ this period is roughly half the period of the pitching motion; i.e., $T \approx \pi$. Other quantities, such as the $z-$component of the force $\hat{C}_z$ (not shown), have the same period $2\pi$ of the pitching motion. This will become clearer from the theoretical approach described in Section 6 below. For the case plotted in Fig. 4 the mean values are $\overline{u} \equiv U \simeq 0.7292$ (we omit in this section the subscript $\infty$ for simplicity), $\overline{\hat{C}}_{xp} \simeq -0.0015$ and $\overline{\hat{C}}_{x\mu} \simeq 0.0015$. Obviously, once $\overline{u}$ has reached a constant value, $\overline{\hat{C}}_x = \overline{\hat{C}}_{xp} + \overline{\hat{C}}_{x\mu} = 0$. The Reynolds number based on $U$ in this case is $Re \simeq 45\,599$ and the Strouhal number $St \simeq 0.087$.

Following Das et al. (2022), it is interesting to characterize the mean swimming velocity $U$ through $Re$ in a $St - Re$ chart. This is made in Fig. 5 for all the cases computed for $R = 0.02$ with different values of the pitch amplitude $\alpha_0$ and frequency $\omega$ (or $Re_\omega$). Note that in order to reach low Reynolds numbers, some of the cases are computed using a higher viscosity than that of water (in particular, $\mu = 0.03134$ kg/ms), for the same $\alpha_0$ and $\omega$. For all values of $\alpha_0$, the numerical results fit quite well the power law $St = 2.75 Re^{-0.375}$ for $Re \lesssim 2000$ (dashed line in Fig. 5). For higher Reynolds numbers the results depend on the pitch amplitude. This Strouhal number's dependence on the Reynolds number agrees with that found by Das et al. (2022), but with a different constant shown with a dash-and-dot line in Fig. 5, with the constant given in the legend, probably due to the use of a NACA0012 airfoil in their numerical simulations instead of the present flat plate. Also, our range of Reynolds numbers is quite different, reaching much higher values of $Re$: here $100 \lesssim Re \lesssim 3 \times 10^5$ vs. $10 \lesssim Re \lesssim 2000$ in Das et al. (2022). That is why we use a transition turbulence model for the numerical simulations. The present range of $Re$, though computationally much more demanding, is more appropriate to compare with the predictions from the inviscid linear theory carried out in the following sections. To that end one has to model appropriately the unsteady viscous drag, not just its time-averaged value, a task undertaken next.

To model the unsteady viscous drag coefficient it is convenient to compare the time evolution $u(t)$, such as that plotted in Fig. 4(a), with the corresponding $\hat{C}_{x\mu}(t)$ [Fig. 4(c)], but normalizing them by subtracting their mean values and dividing by the corresponding amplitudes. This is made in Fig. 6(a) for the last few cycles plotted in Fig. 4. It is observed that both normalized temporal signals almost coincide except for a phase shift. Similarly happens for all the computed cases, the more so the smaller the amplitude $\alpha_0$. Thus, one may write

$$\frac{\hat{C}_{x\mu}(t) - \hat{C}_{D0}}{A_c} \approx \frac{u(t-\phi) - U}{A_u}\,, \tag{12}$$

where we have named $\hat{C}_{D0} \equiv \overline{\hat{C}}_{x\mu}$ the time-averaged viscous drag coefficient, $A_c$ and $A_u$ are the time-averaged amplitudes of the oscillations of the viscous drag and swimming velocity, respectively, and $\phi$ is the phase shift, all of them functions of $\alpha_0$, $Re_\omega$ and $R$, for given $a = -1$. Consequently, the unsteady viscous drag coefficient can be modeled as

$$\hat{C}_{x\mu}(t) \approx \hat{C}_{D0} + \hat{C}_{Du}[u(t-\phi) - U]\,, \qquad \hat{C}_{Du} \equiv \frac{A_c}{A_u}\,. \tag{13}$$

This is then the approximate relation of $\hat{C}_{x\mu}$ with time $t$, through $u(t)$, and with the mean velocity $U$. It remains to characterize $\hat{C}_{D0}$, $\hat{C}_{Du}$ and $\phi$ in terms of the non-dimensional parameters $\alpha_0$, $Re_\omega$ and $R$. To that end, $5 \times 8$ numerical simulations for $R = 0.02$ with 5 different values of $\alpha_0$ and 8 different $Re_\omega$ for each $\alpha_0$ have been performed (the results for the time-averaged velocity $U$ of these simulations in the $Re - St$ plane are compiled in Fig. 5). Additional numerical simulations for $R = 0.01$ and $R = 0.04$ have been made for selected values of $\alpha_0$ and $Re_\omega$. From all these numerical data it turns out that all the parameters, $\hat{C}_{D0}$, $\hat{C}_{Du}$, $U$ and $\phi$, are practically independent of the mass ratio $R$, provided that $R$ remains small, which is the case in flapping propulsion in water. On the other hand, it is found that $\hat{C}_{Du}$ is also practically independent of the pitch amplitude $\alpha_0$, that it follows a power law with $Re_\omega$ in a wide range of values of $Re_\omega$, and that $\phi$ remains practically constant for all the values of $\alpha_0$ and $Re_\omega$ considered. These results for $\hat{C}_{Du}$ and $\phi$ are displayed in Fig. 7 and can be summarized with the following expressions:

$$\hat{C}_{Du} \approx 1.45\, Re_\omega^{-0.46}\,, \qquad 2 \times 10^3 \lesssim Re_\omega \lesssim 5 \times 10^4\,, \tag{14}$$

$$\phi \approx 17^\circ\,, \qquad Re_\omega \lesssim 10^5\,. \tag{15}$$

Finally, the dependence of the time-averaged viscous drag $\hat{C}_{D0}$ with $\alpha_0$ and $Re_\omega$ does not follow simple powers laws. It does however with $U$ and, therefore, with the Reynolds number $Re$ based on $U$, especially when the standard drag coefficient scaled with the squared velocity, $C_{D0} = \pi \hat{C}_{D0}/U^2$ [see Eq. (5)] is used, where $C_{D0} \equiv \overline{C}_{x\mu}$. Fig. 8 shows that this time-averaged viscous drag coefficient can be approximated by power laws of both $Re$ and $\alpha_0$ in an ample range of Reynolds numbers of interest for aquatic propulsion:

$$C_{D0} \approx 5.7\, Re^{-0.71} \alpha_0^{-0.4}\,, \qquad 500 \lesssim Re \lesssim 2 \times 10^4\,. \tag{16}$$

It must be noted that the Reynolds numbers here are significantly larger than in most previous studies dealing with the skin friction on a flapping foil (Ehrenstein and Eloy, 2013; Ehrenstein et al., 2014; Das et al., 2016, 2022; Gross et al., 2021). These computationally works for $Re \lesssim 10^3$ confirmed the Bone-Lighthill boundary layer thinning hypothesis for uniform flow past oscillatory plates, with skin friction drag coefficients proportional to $Re^{-1/2}$, like in Blasius flat plate, but multiplied by a factor proportional to the square root of the ratio of the transverse and longitudinal velocities. Labasse et al. (2020) considered $Re = 2000$ for different $\alpha_0$, finding that Blasius-type scaling is not reliable, without providing any scaling law. Gross et al. (2021) also considered the range $Re \gtrsim 10^3$–$10^4$, but neglected the viscous drag for these larger Reynolds numbers, considering only a constant *pressure* drag coefficient. Here, we use the expression (16) for the time-average viscous drag, while all the pressure forces, of any sign, will be modeled with analytical expressions from linear inviscid theory (Section 5 below). The numerical results will corroborate this choice for the pressure forces in the present Reynolds number's range, provided that $\alpha_0$ is small enough, as previously found in the comparison with experimental data for a pitching foil immersed in a uniform current, both for time-averaged and instantaneous thrust forces (Fernandez-Feria, 2017; Fernandez-Feria and Sanmiguel-Rojas, 2019; Alaminos-Quesada, 2021).

In summary, in a wide range of Reynolds numbers of interest and for small pitch amplitude, the viscous drag, which in what follows will be

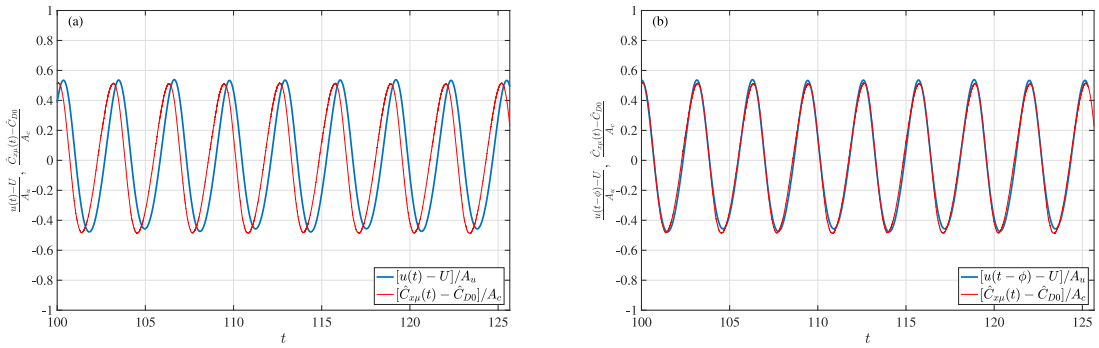


**Fig. 6.** (a) Last cycles of the time evolutions of $(u-U)/A_u$ (thick blue line) and $(\hat{C}_{x\mu}-C_{D0})/A_c$ (thin red line) for the same case plotted in Fig. 4. (b) The same figure but for a phase shift $\phi \simeq 0.340$ in $u(t)$. $A_c \simeq 0.0032$, $A_u \simeq 0.274$, $\hat{C}_{D0} \simeq 0.0015$, $U \simeq 0.7292$. (For interpretation of the references to color in this figure legend, the reader is referred to the web version of this article.)

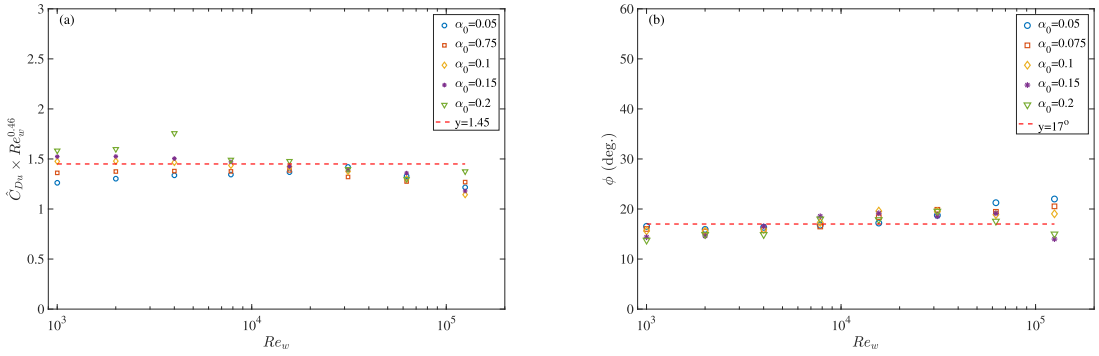


**Fig. 7.** Scaled $\hat{C}_{Du}$ (a) and $\phi$ (b) vs. $Re_\omega$ for different $\alpha_0$. $R = 0.02$.

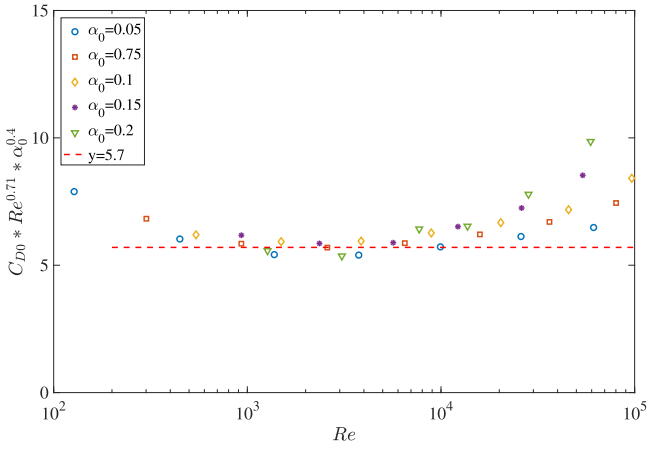


**Fig. 8.** Scaled $C_{D0}$. $R = 0.02$.

termed as $\hat{C}_D$, can be approximated by the following expression (note that Eq. (10) is used to relate $Re$ with $Re_\omega$ and $U$):

$$\hat{C}_D(t) \equiv \hat{C}_{x\mu}(t) \approx C_0 Re_\omega^{-a_0} \alpha_0^{-b_0} U^{c_0} + C_1 Re_\omega^{-a_1} [u(t-\phi) - U]\,, \tag{17}$$

where

$$C_0 \simeq 1.1\,, \quad a_0 \simeq 0.71\,, \quad b_0 \simeq 0.4\,, \quad c_0 \simeq 1.29\,, \quad C_1 \simeq 1.45\,,$$
$$a_1 \simeq 0.46\,, \quad \phi \simeq 0.30\,. \tag{18}$$

All the above numerical results are for a pivot point located at the leading edge, $a = -1$. When it departs from the leading edge, the numerical values of the above expressions would change. For that reason, (17) will be used in the following section in general, without specifying the numerical values of the constants. However, when comparing with the numerical results, obtained for $a = -1$, obviously the values given in (18) will be used.

## 5. Self-propulsion models with thrust from linear potential theory

If the fluid flow is assumed inviscid and the pitch amplitude is small, $|\alpha| \ll 1$, the thrust force generated by the pressure acting on the pitching foil surface can be obtained analytically. The resulting thrust coefficient $\hat{C}_T(t)$ corresponds to $-\hat{C}_x(t)$ but neglecting viscous forces. To close the self-propulsion problem in this near-inviscid limit we add the model of the viscous drag coefficient $\hat{C}_D(t)$ given by (17), so that Eq. (3) becomes

$$R\dot{u} = \hat{C}_T - \hat{C}_D\,. \tag{19}$$

Two alternative expressions for the thrust coefficient are used, that obtained by Garrick (1936) from Theodorsen's theory (Theodorsen, 1935), $\hat{C}_T^G(t)$, and the result from the linearized vortical impulse theory (Fernandez-Feria, 2016), $\hat{C}_T^F(t)$. Both contains the same term $-\alpha\hat{C}_L(t)$, where $\hat{C}_L(t)$ is Theodorsen's lift force non-dimensionalized with the present scaling, modified by Greenberg (1947) with an additional added mass term proportional to $\dot{u}$ to account for the pulsating stream, and with Theodorsen's function appearing in the circulatory terms evaluated at variable $k(t) = 1/u(t)$. In the present notation, and when only the pitching motion is considered, it can be written as

$$\hat{C}_L(t) = -a\ddot{\alpha} + u\dot{\alpha} + \dot{u}\alpha + \Re[C(k)]u\Gamma_0(t)\,, \tag{20}$$

$$\Gamma_0(t) = -2\left[\left(a - \frac{1}{2}\right)\dot{\alpha} - u\alpha\right]\,, \tag{21}$$

where

$$C(k) = \frac{H_1^{(2)}(k)}{iH_0^{(2)}(k) + H_1^{(2)}(k)} = \mathcal{F}(k) + i\mathcal{G}(k) \tag{22}$$

is Theodorsen's function and $\mathfrak{R}$ means real part. However, the remaining terms of the thrust coefficient are different in both formulations. For pitching only and in the present notation they can be written as (Garrick, 1936; Fernandez-Feria, 2016):

$$\hat{C}_T^G(t) = -\alpha\hat{C}_L + \frac{1}{2}\left\{\mathfrak{R}[C(k)]\Gamma_0 - \dot{\alpha}\right\}^2 , \tag{23}$$

$$\hat{C}_T^F(t) = -\alpha\hat{C}_L + \dot{\alpha}\,(a\dot{\alpha} - u\alpha) + \Gamma_0\left\{\mathfrak{R}\left[\frac{2iC_1(k)}{\pi}\right][2\alpha u + (1-a)\dot{\alpha}] - \mathfrak{R}\,[C(k)]\,u\alpha\right\} , \tag{24}$$

where

$$C_1(k) = \frac{\frac{1}{k}e^{-ik}}{iH_0^{(2)}(k) + H_1^{(2)}(k)} = F_1(k) + iG_1(k)\,. \tag{25}$$

After substituting any of these expressions, together with (17) and the pitching motion

$$\alpha(t) = \alpha_0 \sin t \tag{26}$$

into (19), the resulting ODE for $u(t)$ is solved numerically using Matlab's solver ode23, starting from $u(0) = 0$. The corresponding problem with Garrick's thrust $\hat{C}_T^G$ is equivalent to the minimal self-propulsion model of Sánchez-Rodríguez et al. (2020), but with a quite different unsteady model for the skin friction coefficient $\hat{C}_D(t)$, and somewhat simpler because the heaving motion has been inhibited to facilitate the comparison with numerical simulation from the full N–S equations.

A note of caution should be made about the temporal approximations in the thrust and drag coefficients. $\hat{C}_T$ is obtained theoretically using the pressure field from the linear potential theory for a pitching foil in a uniform flow, while $\hat{C}_D$ is obtained by adjusting numerical results of the viscous forces once a final oscillatory motion with constant time-averaged swimming velocity $U_\infty$ has been reached. But both will be used as an approximation during all the oscillatory motion of the foil starting from rest with the local values of $u$ and $U$. This means that for the transient between the initial condition and the final oscillatory state the results of the present model will be merely qualitative. Good for estimating the duration of the transient and the order of magnitude of the velocity peaks, but not for the details of $u(t)$. However, the model should work quantitatively for the final oscillatory state.

## 6. Approximate analytical solutions

Alternatively to the numerical solution of the model equation (19) with (17) and (23) or (24), one may take advantage of the small pitch amplitude, $\alpha_0 \ll 1$, to obtain an analytical approximation for $u(t)$. For small $\alpha_0$, the thrust force is small and, consequently, the non-dimensional swimming velocity will presumably be small too ($u \ll 1$). On the other hand, $u(t)$ may be decomposed into an oscillatory component in the time scale $t$ and a mean part evolving in a much slower time $\tau$. Thus, one may assume

$$u \approx \gamma w(t) + U_\infty W(\tau)\,, \quad \tau = \lambda t\,, \quad \gamma \ll 1\,, \quad U_\infty \ll 1\,, \quad \lambda \ll 1\,, \tag{27}$$

where $w$ and $W$ are order-of-unity functions of their respective arguments, $W \to 1$ for $\tau \gg 1$, the oscillatory function $w(t)$ with zero mean,

$$\overline{w} = 0\,, \quad U_\infty W(\tau) \equiv U(\tau)\,, \tag{28}$$

and the small parameters $\gamma$, $U_\infty$ and $\lambda$ to be determined from the equation of motion for each thrust model. Since $u$ is assumed small, $k = u^{-1} \gg 1$, and one may use the large-$k$ approximation of the functions (22) and (25) (e.g., Fernandez-Feria and Sanmiguel-Rojas, 2019),

$$\mathfrak{R}[C(k)] = \frac{1}{2} + O(k^{-2})\,, \quad \mathfrak{R}\left[\frac{2iC_1(k)}{\pi}\right] = \frac{1}{(4\pi k)^{1/2}} + O(k^{-3/2})\,, \tag{29}$$

to write

$$\hat{C}_T^G \sim \alpha_0^2\frac{1}{4}\left[\left(a-\frac{1}{2}\right)^2 + \left(a^2+3a+\frac{1}{4}\right)\cos(2t)\right] + O(\alpha_0^2 u)\,, \tag{30}$$

$$\hat{C}_T^F \sim \alpha_0^2 a\cos(2t) + \alpha_0^2\frac{u^{1/2}}{2\sqrt{\pi}}\left(a-\frac{1}{2}\right)(a-1)[1+\cos(2t)] + O(\alpha_0^2 u)\,. \tag{31}$$

Using (17) and any of these two thrust models, the equation of motion (19) can then be approximated by

$$R\left(\gamma\frac{dw}{dt} + \lambda U_\infty\frac{dW}{d\tau}\right) \approx \hat{C}_T - C_0 Re_\omega^{-a_0}\alpha_0^{-b_0}(U_\infty W)^{c_0} - C_1 Re_\omega^{-a_1}\gamma\, w(t-\phi)\,. \tag{32}$$

In the following subsections this equation will be solved using the thrust models (30) and (31), respectively, at the lowest order in the small parameters.

### 6.1. Thrust model (30)

Taking the time average of (32) locally at each $\tau$ when using (30) for $\hat{C}_T$, one obtains the following approximate equation for $W(\tau)$:

$$R\lambda U_\infty\frac{dW}{d\tau} \approx \frac{\alpha_0^2}{4}\left(a-\frac{1}{2}\right)^2 - C_0 Re_\omega^{-a_0}\alpha_0^{-b_0}(U_\infty W)^{c_0}\,. \tag{33}$$

Thus, one may select $U_\infty$ and $\lambda$ such that

$$R\lambda U_\infty = \frac{\alpha_0^2}{4}\left(a-\frac{1}{2}\right)^2 = C_0 Re_\omega^{-a_0}\alpha_0^{-b_0}U_\infty^{c_0}\,, \tag{34}$$

so that

$$\frac{dW}{d\tau} = 1 - W^{c_0}\,. \tag{35}$$

This approximation is valid provided that

$$U_\infty = \left[\frac{(a-1/2)^2\alpha_0^{2+b_0}Re_\omega^{a_0}}{4C_0}\right]^{1/c_0} \ll 1\,, \quad \lambda = \frac{\alpha_0^2(a-1/2)^2}{4RU_\infty} \ll 1\,. \tag{36}$$

These requirements obviously limit the validity range of the present approximation in terms of the pitch amplitude $\alpha_0$ and the Reynolds $Re_\omega$. Eq. (35) has to be solved with an initial condition $W(0) = W_0$ (e.g., $W_0 = 0$), and always satisfies $W \to 1$ as $\tau \to \infty$ if $c_0 > 0$ (remember that $c_0 \simeq 1.29$ for $a = -1$). Thus, $U_\infty$ given by the first expression in (36) constitutes an analytical approximation to the final (time-averaged) swimming velocity when Garrick's thrust is used. If $c_0 = 2$ and $W_0 = 0$ the solution of (35) would be simply $W = \tanh\tau$. In general, the solution satisfying $W(0) = 0$ can be written in implicit form as

$$\tau = W\,F[1, 1/c_0; 1/c_0 + 1, W^{c_0}]\,, \tag{37}$$

where $F$ is Gauss' hypergeometric function (Olver et al., 2010).

On the other hand, subtracting (33) to (32) when using (30) for $\hat{C}_T$, the equation for $w(t)$ can be written, at the lowest order, as

$$R\gamma\frac{dw}{dt} \approx \frac{\alpha_0^2}{4}\left(a^2+3a+\frac{1}{4}\right)\cos(2t) - C_1 Re_\omega^{-a_1}\gamma\, w(t-\phi)\,. \tag{38}$$

Selecting

$$\gamma = \frac{\alpha_0^2}{4R}\left(a^2+3a+\frac{1}{4}\right)\,, \quad |\gamma| \ll 1\,, \tag{39}$$

the equation simplifies to

$$\frac{dw}{dt} \approx \cos(2t) - Cw(t-\phi)\,, \qquad C = \frac{C_1 Re_\omega^{-a_1}}{R}\,, \tag{40}$$

whose solution satisfying $w(0) = 0$ is

$$w = \frac{1}{4+C^2}\left\{2\sin(2t) + C\left[\cos(2t) - e^{-Ct}\right]\right\}\,. \tag{41}$$

For $C \ll 1$ this solution can be approximated by $\sin(2t)/2$. In is observed that the oscillatory swimming velocity has a period of $\pi$ in this

approximation, half that of the forced pitching motion, a consequence of the thrust models.

Substituting the functions $w(t)$ and $W(\lambda t)$ into (27) yields the approximate solution with Garrick's thrust, which will be compared in Section 7 below with both numerical solutions, that from the complete FSI problem and the other one from the ODE (19) with (23) and (17). But, independently of the particular functions $w$ and $W$, the present approximate analytical solution provides directly the final, time-averaged swimming velocity $U_\infty$, the amplitude of the final oscillations, about $\gamma/2$, and the order of magnitude $\lambda^{-1}$ of the non-dimensional transient time to reach that final state.

### 6.2. Thrust model (31)

Now, assuming further that $\gamma/U_\infty$ is small, the time-averaged equation is

$$R\lambda U_\infty \frac{dW}{d\tau} \approx \frac{\alpha_0^2}{2\sqrt{\pi}}(a-1/2)(a-1)(U_\infty W)^{1/2} - C_0 Re_\omega^{-a_0}\alpha_0^{-b_0}(U_\infty W)^{c_0}\,. \tag{42}$$

If

$$U_\infty = \left[\frac{(a-1/2)(a-1)\alpha_0^{2+b_0}Re_\omega^{a_0}}{2C_0\sqrt{\pi}}\right]^{1/(c_0-0.5)} \ll 1\,,$$
$$\lambda = \frac{\alpha_0^2(a-1/2)(a-1)}{2R\sqrt{\pi U_\infty}} \ll 1\,, \tag{43}$$

the equation for $W(\tau)$ reads

$$\frac{dW}{d\tau} = W^{1/2}(1 - W^{c_0-1/2})\,. \tag{44}$$

$W$ always tends to unity as $\tau \to \infty$ if $c_0 > 1/2$, as it is the case. The solution of (44) that satisfies $W(0) = 0$ can formally be written in implicit form as

$$\tau = 2\,\frac{W^{c_0} - W^{1/2}}{W^{c_0-1/2}-1}\,F[1, 1/(2(c_0-1/2)); 1/(2(c_0-1/2))+1, W^{c_0-1/2}]\,, \tag{45}$$

where $F$ is again Gauss' hypergeometric function.

Finally, if one defines

$$\gamma = \frac{\alpha_0^2 a}{R}\,, \quad |\gamma| \ll 1\,, \tag{46}$$

the equation for $w$ is the same as (40) in first approximation, so that the solution is also (41). But now, the amplitude $\gamma$ of the oscillations of $u$ is slightly different, though both proportional to $\alpha_0^2/R$. However, the dependencies of the mean forward speed $U_\infty$ and the transient non-dimensional time $\lambda$ on $\alpha_0$ and $Re_\omega$ are quite different, though, as we shall see in the next section, the results are quantitatively very similar within the (narrow) range of validity of the approximations.

## 7. Assessment

Fig. 9 compares $u(t)$ for a particular case ($\alpha_0 = 0.075$ and $Re_\omega = 2000$, with $R = 0.02$ and $a = -1$) obtained from the five approaches described in the preceding sections: full numerical solution, and using the two thrust models, both integrating numerically (19) and using their respective approximate solutions (27). The approximate solutions are in close agreement with the numerical solution of the model equations for both thrust models in this case. As expected, the transient evolutions from the models and the numerical simulation differ substantially, but the final mean values $U_\infty$ are not so different from the numerical simulation in this case, especially when using $\hat{C}_T^F$ in the model. The oscillation amplitude of the swimming velocity, however, is larger than that obtained with the numerical simulation.

Similar trends are observed for other small values of $\alpha_0$ if $Re_\omega \lesssim 10^4$. Obviously, the best agreement for the mean swimming velocity $U_\infty$ is found for the smallest pitch amplitude considered, $\alpha_0 = 0.05$ [see Fig. 10(a)]. The agreement becomes poorer as $\alpha_0$ increases, especially for the higher values of $Re_\omega$. In fact, already for $\alpha_0 = 0.1$, the approximation is only acceptable for the smallest value of the Reynolds number considered, $Re_\omega = 1000$ [Fig. 10(c)]. For larger $Re_\omega$, $U_\infty$ from the model becomes close to, or even larger than, unity and the approximation fails. In most cases considered, the approximation with $\hat{C}_T^F$ works better for the smaller values of $Re_\omega$ [like for instance the case plotted in Fig. 9, included in Fig. 10(b)], while the model with $\hat{C}_T^G$ is a less bad approximation for the larger values $Re_\omega$ in the range $10^3$–$10^4$ considered in Fig. 10. For $\alpha_0 > 0.1$ (not shown in Fig. 10) $U_\infty$ from the models is larger than unity for most $Re_\omega$ considered, and the approximation fails.

The limited pitch amplitude range of validity of the simplified model is imposed by the strong conditions (36), (39), (43) and (46) to be satisfied by the mean velocity $U_\infty$ and the oscillation amplitude $\gamma$ for each thrust model. Namely,

$$\alpha_0 \ll Re_\omega^{-a_0/(b_0+2)} \simeq Re_\omega^{-0.3}\,, \qquad \alpha_0 \ll R^{1/2}\,. \tag{47}$$

Note that the same validity conditions are obtained for both thrust approximations, in spite of the different power laws dependencies of $U_\infty$ on $\alpha_0$ and $Re_\omega$. The first condition explains (and agrees with) the comparison shown in Fig. 10 between the simplified model for $U_\infty$ and the numerical simulations, with the pitch amplitude range of validity decreasing with $Re_\omega$. In fact, this condition predicts that for the case $\alpha_0 = 0.1$ of Fig. 10(c) the model can only provide an approximation at the lowest Reynolds shown in the figure, $Re_\omega \sim 10^3$, while Figs. 10(a) and (b) show that the pitch amplitude validity range becomes negligible small when $Re_\omega$ is well above $10^4$. The second condition (47) is also partly responsible for the poorer agreement in Fig. 10(c) for $\alpha_0 = 0.1$.

## 8. Concluding remarks

Analytical approximations for the non-stationary swimming velocity of a self-propelled pitching foil have been derived using two thrust models from linear potential theory, valid for small pitch amplitude $\alpha_0$, together with an unsteady viscous drag correlation obtained from high-fidelity numerical simulations. These same numerical simulations are used to assess the validity of the model approximation for the swimming velocity over a wide range of frequency based Reynolds numbers, $10^3 \lesssim Re_\omega \lesssim 10^4$. The simplified model is valid in a narrow range of pitch amplitudes that decreases as $Re_\omega$ increases, being negligibly small for $Re_\omega > 10^4$. The mass ratio $R$, which is usually small for flapping locomotion in water, also imposes a limitation on the pitch amplitude for the validity of the simplified model. In particular, using physical magnitudes, the two conditions (47) for the validity of the approximate analytical solutions are

$$\alpha_0\left(\frac{\rho\omega c^2}{4\mu}\right)^{0.3} \ll 1\,, \qquad \alpha_0\left(\frac{\pi\rho c^2}{4m}\right)^{0.5} \ll 1\,. \tag{48}$$

However, numerical solutions of the model equations described in Section 5, without the further requirement of small swimming velocity made in Section 6 leading to the simple analytical solutions, are valid in a wider pitch amplitude range, similar to that described in Alaminos-Quesada (2021) for a pitching foil immersed in a uniform current (i.e., $St \lesssim 0.25$). Nonetheless, the approximate analytical solutions provide quick information about the dependency of the swimming velocity on the different parameters, very useful to start the design of bioinspired underwater vehicles.

Although the swimming velocity predicted by the simplified expressions resulting from both thrust models considered, $\hat{C}_T^G$ and $\hat{C}_T^F$, are quantitatively similar within their common validity range, the power-law dependencies on $\alpha_0$ and $Re_\omega$ are qualitatively different in each model over the Reynolds number range $10^3 \lesssim Re_\omega \lesssim 10^4$. The simplified model for $u(t)$ obtained with $\hat{C}_T^F$ works slightly better for very small $\alpha_0$ over all $Re_\omega$ range, and in the band closer to $Re_\omega = 10^3$ as $\alpha_0$ increases, while the model with $\hat{C}_T^G$ works better in the band closer to $Re_\omega = 10^4$ for increasing $\alpha_0$.

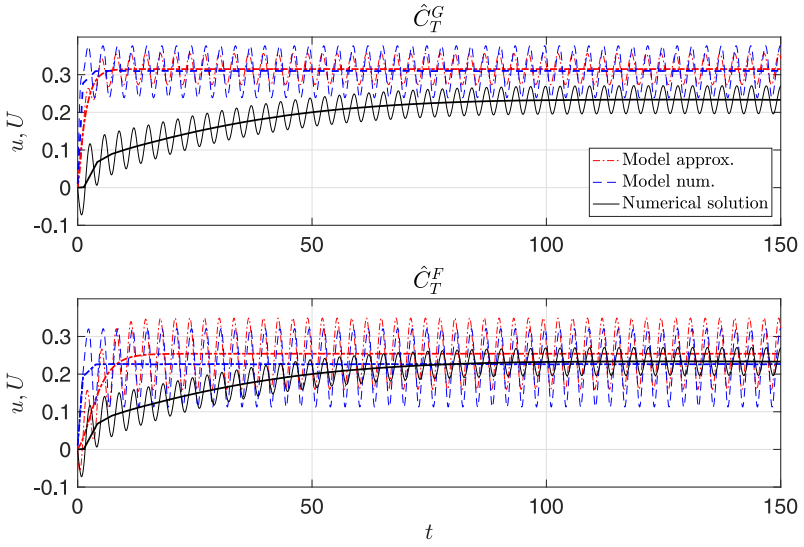


**Fig. 9.** $u(t)$ computed numerically (thin black lines) and its mean $U$ (thick black lines) compared with the model predictions using $\hat{C}_T^G$ (top panel) and $\hat{C}_T^F$ (bottom panel). The numerical solution of the model is plotted with dashed blue lines, and the analytical approximate solution with dash-and-dot red lines. $\alpha_0 = 0.075$, $Re_\omega = 2000$, $R = 0.02$ and $a = -1$. (For interpretation of the references to color in this figure legend, the reader is referred to the web version of this article.)

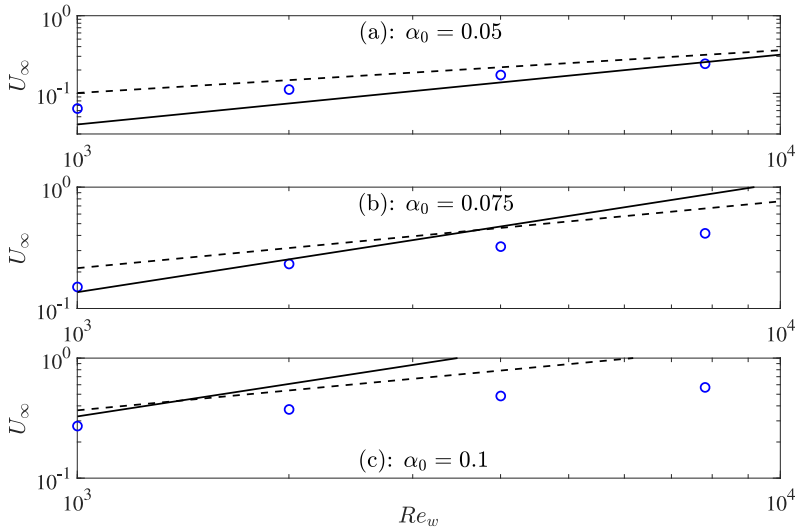


**Fig. 10.** Comparison of $U_\infty$ from the model approximations using $\hat{C}_T^G$ (dashed lines) and $\hat{C}_T^F$ (continuous lines) with numerical results (circles) for three values of $\alpha_0$ and $10^3 \le Re_\omega \le 10^4$. $R = 0.02$ and $a = -1$.

## CRediT authorship contribution statement

**R. Fernandez-Feria:** Conceptualization, Formal analysis, Funding acquisition, Investigation, Methodology, Project administration, Software, Supervision, Validation, Visualization, Writing – original draft, Writing – review & editing. **E. Sanmiguel-Rojas:** Data curation, Formal analysis, Funding acquisition, Investigation, Methodology, Project administration, Supervision, Resources, Software, Validation, Visualization, Writing – review & editing. **P.E. Lopez-Tello:** Data curation, Methodology, Resources, Software, Validation, Visualization, Writing – review & editing.

## Declaration of competing interest

The authors declare that they have no known competing financial interests or personal relationships that could have appeared to influence the work reported in this paper.

## Acknowledgments

This research has been supported by the Junta de Andalucía, Spain (UMA18-FEDER-JA-047 and P18-FR-1532). The computations were performed in the Picasso Supercomputer at the University of Málaga, a node of the Spanish Supercomputing Network.

## Appendix. Details of the numerical approach

Transient, pressure-based, coupled solver with absolute velocity formulation are the settings for the solution of all simulations. The least-squares cell based method is applied for calculating the gradients of the transport quantities on the faces of the cells. The spatial discretization methods in all FSI simulations are solved with second order for the pressure term, and second-order upwind for continuity, momentum and turbulent quantities. The explicit relaxation factors of pressure and momentum are set at 0.75 to ensure the stability of the numerical method. The overset method is used for the moving mesh. First order implicit formulation is applied for discretizing

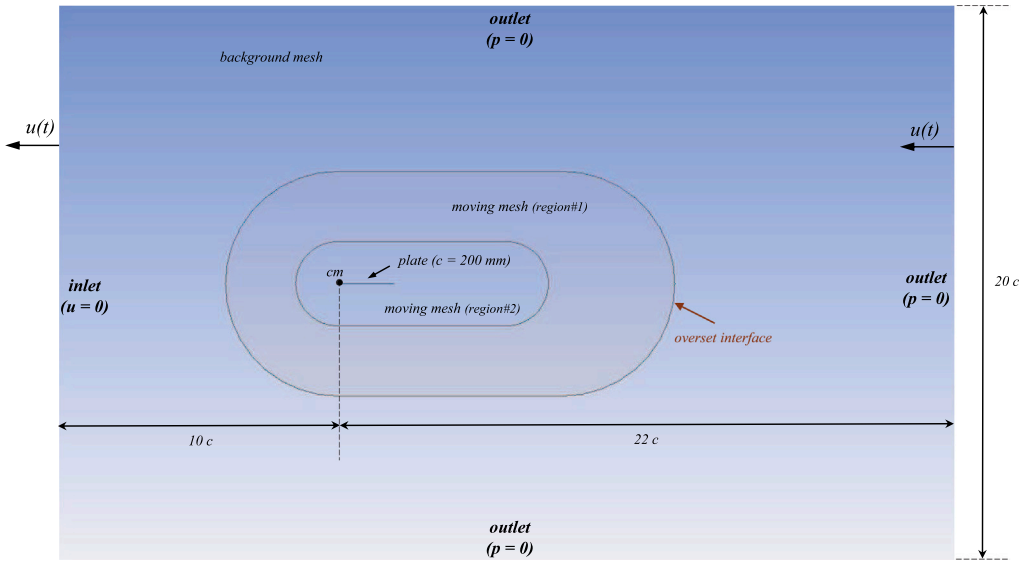


**Fig. A.1.** Computational domain, including subdomains, dimensions and indication of boundary conditions.

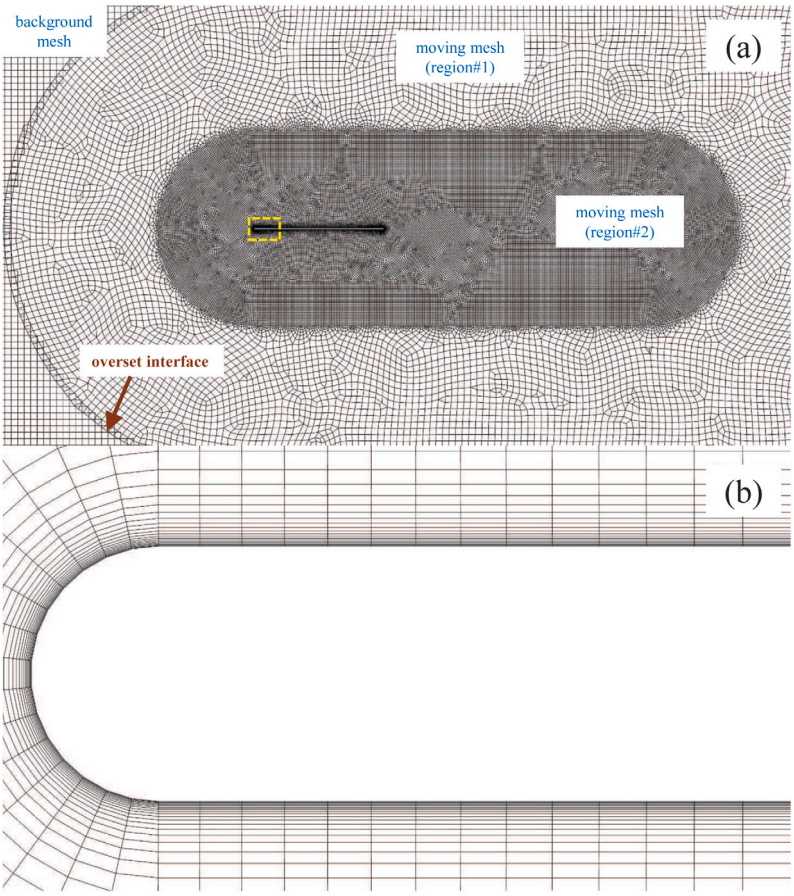


**Fig. A.2.** Two views of mesh #1. (b) is a zoom of the dashed rectangle in (a) containing the plate head.

the time derivatives, in order to accomplish numerical stability for the dynamic mesh algorithm. At each time step, the convergence is considered reached once the absolute residuals values $5 \times 10^{-4}, 10^{-3}$ and $5 \times 10^{-5}$ for continuity, turbulence and momentum quantities are fulfilled, respectively. All simulations start from rest.

Fig. A.1 shows the computational domain (width = $20c$, length = $32c$) used in all simulations. With larger computational domains, the results have practically not changed even in the most computationally demanding cases. The mesh consists of two different regions (see Figs. A.1 and A.2): a background mesh and a mesh moving as a rigid solid with the plate. In order to keep constant the size of the initial computational domain, we use the layering algorithm as dynamic mesh, to destroy (on the right) and to build up (on the left) the background mesh with the velocity $u$ of the center of mass of the

plate (see Fig. A.1). The moving mesh interpolates continuously over the background mesh thanks to the overset interface [see Fig. A.2(a)]. Furthermore, the moving mesh is split into two different regions to ease the meshing procedure around the plate and, at the same time, to ensure a good interpolation procedure over the background mesh at the overset interface. The boundary conditions are indicated in Fig. A.1: the absolute velocity is set to zero at the inlet, at a distance $10c$ upstream the plate; non-slip wall on the foil, and pressure outlet $p = 0$ on the rest of the boundaries.

Both background and moving meshes include only quad cells with a maximum skewness $< 0.6$. In order to capture correctly the boundary layer around the plate, we set an inflation layer of 20 cells with a growth rate 1.2 and the first cell thickness of size $0.007, 0.005$ and $0.0035$ mm for meshes #0, #1 and #2, respectively [see Fig. A.2(b) for mesh #1]. This first layer thickness guarantees a maximum $y^+ < 0.5$ on the foil wall, even for the most demanding case calculated with the coarse mesh#0.

## References


Alaminos-Quesada, J., 2021. Limit of the two-dimensional linear potential theories on the propulsion of a flapping airfoil in forward flight in terms of the Reynolds and Strouhal number. Phys. Rev. Fluids 6 (12), 123101.

Alben, S., Shelley, M., 2005. Coherent locomotion as an attracting state for a free flapping body. Proc. Nat. Acad. Sci. USA 102 (32), 11163–11166.

Alexander, R.M., 2003. Principles of Animal Locomotion. Princeton University Press.

Anderson, J.M., Streitlien, K., Barret, K.S., Triantafyllou, M.S., 1998. Oscillating foils of high propulsive efficiency. J. Fluid Mech. 360, 41–72.

Benetti Ramos, L., Marquet, O., Bergmann, M., Iollo, A., 2021. Fluid-solid Floquet stability analysis of self-propelled heaving foils. J. Fluid Mech. 910 (A28).

Das, A., Shukla, R.K., Govardhan, R.N., 2016. Existence of a sharp transition in the peak propulsive efficiency of a low-Re pitching foil. J. Fluid Mech. 800, 307–326.

Das, A., Shukla, R.K., Govardhan, R.N., 2019. Foil locomotion through non-sinusoidal pitching motion. J. Fluids Struct. 89, 191–202.

Das, A., Shukla, R.K., Govardhan, R.N., 2022. Contrasting thrust generation mechanics and energetics of flapping foil locomotory states characterized by a unified St-Re scaling. J. Fluid Mech. 930 (A27).

Ehrenstein, U., Eloy, C., 2013. Skin friction on a moving wall and its implication for swimming animals. J. Fluid Mech. 718, 321–346.

Ehrenstein, U., Marquillie, M., Eloy, C., 2014. Skin friction on a flapping plate in uniform flow. Phil. Trans. R. Soc. A 372, 20130345.

Eloy, C., 2012. Optimal strouhal number for swimming animals. J. Fluids Struct. 30, 205–218.

Fernandez-Feria, R., 2016. Linearized propulsion theory of flapping airfoils revisited. Phys. Rev. Fluids 1, 084502.

Fernandez-Feria, R., 2017. Note on optimum propulsion of heaving and pitching airfoils from linear potential theory. J. Fluid Mech. 826, 781–796.

Fernandez-Feria, R., Sanmiguel-Rojas, E., 2019. Comparison of aerodynamic models for two-dimensional pitching foils with experimental data. Phys. Fluids 31, 057104.

Floryan, D., Van Buren, T., Rowley, C.W., Smits, A.J., 2017. Scaling the propulsive performance of heaving and pitching foils. J. Fluid Mech. 822, 386–397.

Garrick, I.E., 1936. Propulsion of a Flapping and Oscillating Airfoil. Tech. Rep. TR 567, NACA.

Gazzola, M., Argentina, M., Mahadevan, L., 2014. Scaling macroscopic aquatic locomotion. Nat. Phys. 10, 758–761.

Gibouin, F., Raufaste, C., Bouret, Y., Argentina, M., 2018. Study of the thrust-drag balance with a swimming robotic fish. Phys. Fluids 30 (9), 091901.

Greenberg, J.M., 1947. Airfoil in Sinusoidal Motion in a Pulsating Stream. Tech. Rep. TR 1326, NACA.

Gross, D., Roux, Y., Raufaste, C., Argentina, M., 2021. Drag analysis with a self-propelled flexible swimmer. Phys. Rev. Fluids 6, 053101.

Kang, C.K., Baik, Y.S., Bernal, L., Ol, M.V., Shyy, W., 2009. Fluid dynamics of pitching and plunging airfoils of Reynolds number between $1 \times 10^4$ and $6 \times 10^4$. In: AIAA Paper. pp. 2009–536.

Karbasian, H.R., Kim, K.C., 2016. Numerical investigations on flow structure and behavior of vortices in the dynamic stall of an oscillating pitching hydrofoil. Ocean Eng. 127, 200–211.

Labasse, J., Ehrenstein, U., Meliga, P., 2020. Numerical exploration of the pitching plate parameter space with application to thrust scaling. Appl. Ocean Res. 101, 102278.

Lauder, G.V., Anderson, E.J., Tangorra, J., Madden, P.G.A., 2007. Fish biorobotics: Kinematics and hydrodynamics of self-propulsion. J. Exp. Biol 210, 2767–2780.

Lighthill, M.J., 1969. Hydromechanics of aquatic animal propulsion. Ann. Rev. Fluid Mech. 1, 413–449.

Lighthill, M.J., 1970. Aquatic animal propulsion of high hydromechanical efficiency. J. Fluid Mech. 44, 265–301.

Lin, X., Wu, J., Zhang, T., 2021. Self-directed propulsion of an unconstrained flapping swimmer at low Reynolds number: hydrodynamic behaviour and scaling laws. J. Fluid Mech. 907 (R3).

Mackowski, A.W., Williamson, C.H.K., 2015. Direct measurement of thrust and efficiency of an airfoil undergoing pure pitching. J. Fluid Mech. 765, 524–543.

Olver, F.W.J., Lozier, D.W., Boisvert, R.F., Clark, C.W. (Eds.), 2010. NIST Handbook of Mathematical Functions. Cambridge University Press, Cambridge, (UK).

Paniccia, D., Padovani, L., Graziani, G., Piva, R., 2021. The performance of a flapping foil for a self-propelled fishlike body. Sci. Rep. 11 (22297).

Saadat, M., Fish, F.E., Domel, A.G., Santo, V.Di., Lauder, G.V., Haj-Hariri, H., 2017. On the rules for aquatic locomotion. Phys. Rev. Fluids 2, 083102.

Sánchez-Rodríguez, J., Celestini, F., Raufaste, C., Argentina, M., 2021. Proprioceptive mechanism for bioinspired fish swimming. Phys. Rev. Lett. 126, 234501.

Sánchez-Rodríguez, J., Raufaste, C., Argentina, M., 2020. A minimal model of self propelled locomotion. J. Fluids Struct. 97, 103071.

Sanmiguel-Rojas, E., Fernandez-Feria, R., 2021. Propulsion enhancement of flexible plunging foils: Comparing linear theory predictions with high-fidelity CFD results. Ocean Eng. 235, 109331.

Sanmiguel-Rojas, E., Fernandez-Feria, R., 2022. Numerical study of the propulsive performance of two-dimensional pitching foils at very high frequencies: Scaling laws and turbulence effects. Int. J. Numer. Methods Heat Fluid Flow 32, 1602–1617.

Smits, A.J., 2019. Undulatory and oscillatory swimming. J. Fluid Mech. 874, 1–70, P1.

Spagnolie, S.E., Moret, L., Shelley, M.J., Zhang, J., 2010. Surprising behaviors in flapping locomotion with passive pitching. Phys. Fluids 22 (4), 041903.

Taylor, G.K., Nudds, R.L., Thomas, A.L.R., 2003. Flying and swimming animals cruise at a Strouhal number tuned for high power efficiency. Nature 425, 707–711.

Theodorsen, T., 1935. General Theory of Aerodynamic Instability and the Mechanism of Flutter. Tech. Rep. TR 496, NACA.

Triantafyllou, M.S., Hover, F.S., Techet, A.H., Yue, D.K.P., 2005. Review of hydrodynamic scaling laws in aquatic locomotion and fishlike swimming. Appl. Mech. Rev. 7, 226–237.

Triantafyllou, M.S., Triantafyllou, G.S., 1995. An efficient swimming machine. Sci. Am. 1995, 64–70.

Triantafyllou, M.S., Triantafyllou, G.S., Gopalkrishnan, R., 1991. Wake mechanics for thrust generation in oscillating foils. Phys. Fluids A 3, 2835–2837.

Triantafyllou, G.S., Triantafyllou, M.S., Grosenbaugh, M.A., 1993. Optimal thrust development in oscillating foils with application to fish propulsion. J. Fluid Struct. 7, 205–224.

Webb, P.W., 1975. Hydrodynamics and energetics of fish propulsion. Bull. Fish. Res. Board Can. 190, 1–158.

Wen, L., Wang, T.M., Wu, G.H., Liang, J.H., 2012. Hydrodynamic investigation of a self- propelled robotic fish based on a force-feedback control method. Bioinsp. Biomimetics 7, 032012.

Wu, T.Y., 1971. Hydromechanics of swimming propulsion. Part 3. swimming and optimum movements of slender fish with side fins. J. Fluid Mech. 46, 545–568.

Wu, X., Zhang, X., Tian, X., Li, X., Lu, W., 2020. A review on fluid dynamics of flapping foils. Ocean Eng. 195, 106712.

Young, J., Lai, J.C.S., 2007. Mechanisms influencing the efficiency of oscillating airfoil propulsion. AIAA J. 45, 1695–1702.

Zhang, J., Liu, N.S., Lu, X.Y., 2010. Locomotion of a passively flapping flat plate. J. Fluid Mech. 659, 43–68.

Zhu, J., White, C., Wainwright, D.K., Di Santo, V., Lauder, G.V., Bart-Smith, H., 2019. Tuna robotics: A high-frequency experimental platform exploring the performance space of swimming fishes. Sci. Rob. 4 (34), eaax4615.